Composite Structures 131 (2015) 333–343

Contents lists available at ScienceDirect

Composite Structures

journal homepage: www.elsevier.com/locate/compstruct

XFEM buckling analysis of cracked composite plates

Amir Nasirmanesh, Soheil Mohammadi *

High Performance Computing Lab, School of Civil Engineering, University of Tehran, Tehran, Iran

ARTICLE INFO

Article history:
Available online 13 May 2015

Keywords:
Buckling analysis
Extended finite element method (XFEM)
Crack
Composite plate
Orthotropic tip enrichment functions

ABSTRACT

Linear eigenvalue buckling analysis for cracked uni-layer composite plates is performed in the framework of the extended finite element method (XFEM). The geometry of the problem is discretized using the 8-noded degenerated shell element, which includes transverse shear deformation effects. The effects of several parameters such as crack lengths and angles, fiber directions and boundary conditions on the buckling behavior of cracked composite plates are comprehensively investigated for different loading conditions including compressive, tensile and shear loadings. Also, the accuracy and efficiency of the proposed method are discussed and compared with the available results.

1. Introduction

Composite materials have been widely used in aerospace, marine and civil engineering in the form of thin plate structures due to their advantages such as the high ratio of strength to weight. Among several different failure modes for thin composite plates, the buckling failure can jeopardize the overall safety of the structure due to sudden and large deformations that occur. In general, structural components, especially thin plates are highly susceptible to buckling when they are subjected to compressive loadings. Nevertheless, the presence of flaws such as cracks in plates can cause local and even global buckling even in tensile loadings. As a result, the presence of imperfections, such as cracks, voids and etc, during manufacturing, installation and performance not only reduces the stiffness and strength of plate, they highly increase the risk of buckling even in tensile loadings by creating local multi-axial and compressive stress states around the crack.

A number of studies are available on buckling analysis of composite and orthotropic plates without cracks. Thai and Kim [1] presented the closed-form solution for buckling of rectangular orthotropic plates. They assumed a quadratic variation for transverse shear strains across the thickness. Lopatin and Morozof [2] studied the buckling of rectangular orthotropic composite plates subjected to a linearly distributed in-plane loading using the two-variable refined theory. They investigated the effect of aspect ratio and direction of fibers on the buckling behavior and determined the optimum angle of fibers. Similar studies [3–6] were performed on the buckling analysis of orthotropic composite plates. Also, several studies have been performed for the analysis of composite plates in the framework of the isogeometric analysis, which is capable of modeling complex geometries [7–9].

On the other hand, many researchers have studied the buckling of cracked isotropic plates. For instance, Markström and Stoakers [10] performed a finite element analysis to study buckling of cracked members under tension, and concluded that the critical buckling stress was proportional to the square of the crack length, inversely. A similar study was performed in [11] using singular tip elements. Riks et al. [12] demonstrated that the stress intensity factors increased around the crack tips dramatically when buckling occurred. The integral equation method was applied by Vafai et al. [13] to study the edge cracked plates under in-plane compressive periodic loading. Experimental and numerical buckling analysis of isotropic cracked rectangular plates under compressive and tensile loading were performed by Seifi and Kabiri [14] and Seifi and Khoda-yari [15], while shear buckling and post-buckling analysis of cracked panels were studied by Alinia et al. [16] using the finite element method. They showed that the accuracy of the results were highly sensitive to mesh density at crack tips. Other works on isotropic plates can be found in [17–20]. Natarajan et al. [21] developed an XFEM model to solve the buckling problem of isotropic cracked plates using a plate element with smooth curvatures. Free vibration analysis of cracked functionally graded plates was performed by Natarajan et al. based on XFEM and using a 4-noded quadrilateral plate element [22]. They investigated the effect of crack length, crack location, crack orientation, gradient index of material and the thickness of plate on the natural frequencies and mode shapes of the plate. Recently, Nguyen-Thoi et al. [23] studied the problem of free vibration analysis of cracked Mindlin plates using the extended cell-based smoothed discrete shear gap

* Corresponding author. Tel.: +98 21 6111 2258; fax: +98 21 6640 3808.
E-mail address: smoham@ut.ac.ir (S. Mohammadi).

http://dx.doi.org/10.1016/j.compstruct.2015.05.013
0263-8223/

method (XCS-DSG3). They concluded that the proposed method had a high accuracy in comparison to other conventional plate elements. Another study about extended discrete shear gap method can be found in [24].

There is, however, only a very limited literature on the buckling analysis of cracked orthotropic plates. Barut et al. [25] presented a numerical study on buckling and post-buckling of laminated composite plates with an inclined crack subjected to tension using a geometrical nonlinear finite element method. The effect of layer sequence on the critical buckling stress was also studied. In their proposed method, elements should conform to crack faces, preventing simulation of arbitrary crack propagations. Recently, Rad and Panahandeh-Shahraki [26] studied the buckling of functionally graded plates subjected to uni-axial and bi-axial tensile loads by means of the finite element method. They concluded that the buckling load decreased by the increase of gradient index of material and this attitude was more sensitive for bi-axial loadings. Similarly, a parametric study was performed, using partition of unity method, to investigate the effect of discontinuities in the functionally graded material plates [27], showing that with increasing material gradient index and crack length, the buckling load would decrease. It should be noted that they used isotropic tip enrichment functions for tip elements. None of the existing works has studied the problem of buckling of cracked orthotropic plates subjected to general loading conditions with the extended finite element method. In this study, XFEM is adopted for buckling analysis of several mixed-mode cracked composite plates for the first time. The orthotropic crack tip enrichment functions [28] are considered to model the stress singularity in a more accurate manner.

XFEM has been developed in the past decade to alleviate the shortcomings of the finite element method in discontinuous problems, by avoiding the need of conforming the discontinuity to the mesh edges and also adopting singular elements for reproducing the stress singularity at crack tips. This method has successfully been extended to several static and dynamic isotropic and orthotropic problems, as well as modeling inter laminar cracks in bi-materials [22,28–38]. Recently, Nguyen-Thanh et al. [39] developed an extended isogeometric shell formulation based on the Kirchhoff–Love theory. More advanced methods related to the problem of cracked shells can be found in [40,41]. Also, For a comprehensive review of XFEM developments, see [42,43].

The structure of the paper is as follows: the fundamental equations of the shell element and the buckling eigenvalue equations are discussed in the framework of XFEM formulation with an emphasize on isotropic and orthotropic crack tip enrichment functions. Several numerical examples are presented and discussed in Section 3, beginning with verifications and then extension to orthotropic composite plates. The last part of the paper presents the results for the buckling analysis of various cracked composite plates.

2. Basic formulation

In the present study, eight noded shell elements based on the Mindlin–Reissner theory are used to discretize the model. These elements have many advantages such as avoiding mesh distortion and shear locking in thin plates and shells. The geometry of the shell element is interpolated using

$$\begin{Bmatrix} x \\ y \\ z \end{Bmatrix} = \sum_{i=1}^{n} N_i(\xi,\eta) \begin{Bmatrix} x_i \\ y_i \\ z_i \end{Bmatrix} + \frac{t}{2}\sum_{i=1}^{n} \zeta N_i(\xi,\eta) \begin{Bmatrix} V_{xi}^3 \\ V_{yi}^3 \\ V_{zi}^3 \end{Bmatrix} \tag{1}$$

where t is the thickness of the shell element, $N_i(\xi,\eta)$ are the conventional shape functions in the natural coordinate system, $n = 8$ is the number of nodes in the element, V_i^3 is the unit normal vector at node i and ζ is perpendicular to the mid-surface in the natural coordinate system (Fig. 1).

Taking into account the shear deformation effects, approximation of the displacement field can be expressed in terms of nodal displacements and rotations,

$$\mathbf{u}_{\text{fem}} = \sum_{i=1}^{n} N_i \mathbf{u}_i - \frac{t}{2}\sum_{i=1}^{n} N_i \zeta \mathbf{e}_{xi}\alpha_i + \frac{t}{2}\sum_{i=1}^{n} N_i \zeta \mathbf{e}_{yi}\beta_i \tag{2}$$

where $\mathbf{e}_{xi}$ and $\mathbf{e}_{yi}$ are the orthonormal vectors of unit normal vector at node i, as depicted in Fig. 1, α_i and β_i are rotations with respect to x and y directions, respectively, and

$$\mathbf{u}^T = \{u, v, w\} \tag{3}$$

u, v and w are the displacement components in x, y and z directions, respectively. The standard vector of unknowns $\underset{\sim}{\mathbf{d}}$ is defined as,

$$\underset{\sim}{\mathbf{d}} = \{u, v, w, \alpha, \beta\}^T \tag{4}$$

Now, let us consider a crack in an orthotropic uni-layer composite plate, as shown in Fig. 2. The general form of XFEM approximation for the displacement field of any point $\mathbf{x}$ is defined as:

$$\underset{\sim}{\mathbf{u}} = \mathbf{u}_{\text{fem}} + \mathbf{u}_{\text{enrich}} \tag{5}$$

On the right hand side of this equation, the first part is the conventional finite element approximation and the second part is added in order to consider the crack face discontinuity and the stress singularity at crack tips

$$\mathbf{u}_{\text{enrich}} = \mathbf{u}_{\text{crack-face}} + \mathbf{u}_{\text{crack-tip}} \tag{6}$$

where $\mathbf{u}_{\text{crack-face}}$ enriches the displacement field with the Heaviside function so that the discontinuity along the crack edges is modeled

$$\mathbf{u}_{\text{crack-face}} = \sum_{i=1}^{n} N_i H(\mathbf{x}) \mathbf{a}_i + \frac{t}{2}\sum_{i=1}^{n} \zeta N_i H(\mathbf{x}) \left[-\mathbf{e}_{xi} a_{\alpha i} + \mathbf{e}_{yi} a_{\beta i}\right] \tag{7}$$

where

$$\mathbf{a}_i = \left\{a_i^u, a_i^v, a_i^w\right\}^T \tag{8}$$

It should be noted that $\mathbf{a}_i, a_{\alpha i}$ and $a_{\beta i}$ are the additional enrichment degrees of freedom. The enrichment vector of degrees of freedom $\mathbf{h}$ can be written as,

$$\mathbf{h} = \left\{a_i^u, a_i^v, a_i^w, a_{\alpha i}, a_{\beta i}\right\}^T \tag{9}$$

The Heaviside function for a point $\mathbf{x}$ is defined as [42]

$$H(\mathbf{x}) = \begin{cases} +1 & \mathbf{x} \text{ above the crack} \\ -1 & \mathbf{x} \text{ under the crack} \end{cases} \tag{10}$$

The term $\mathbf{u}_{\text{crack-tip}}$ in Eq. (5) is added to enrich the displacement field to capture the stress singularity at the crack tip,

$$\mathbf{u}_{\text{crack-tip}} = \sum_{i=1}^{nt} N_i \sum_{j=1}^{m} (F_j(\mathbf{x}) - F_j(\mathbf{x}_i)) \begin{Bmatrix} b_i^u \\ b_i^v \\ 0 \end{Bmatrix} + \sum_{i=1}^{nt} N_i \sum_{j=1}^{m} (G_j(\mathbf{x}) - G_j(\mathbf{x}_i)) \begin{Bmatrix} 0 \\ 0 \\ b_i^w \end{Bmatrix} + \sum_{i=1}^{nt} N_i \frac{\zeta t_i}{2} \sum_{j=1}^{m} (R_j(\mathbf{x}) - R_j(\mathbf{x}_i)) \left[-\mathbf{e}_{xi} b_{\alpha i}^j + \mathbf{e}_{yi} b_{\beta i}^j\right] \tag{11}$$

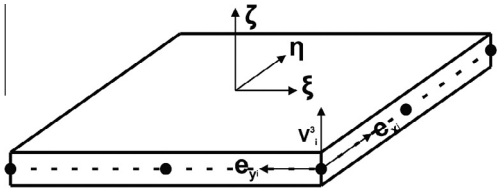

Fig. 1. Geometry of the 8 noded shell element.

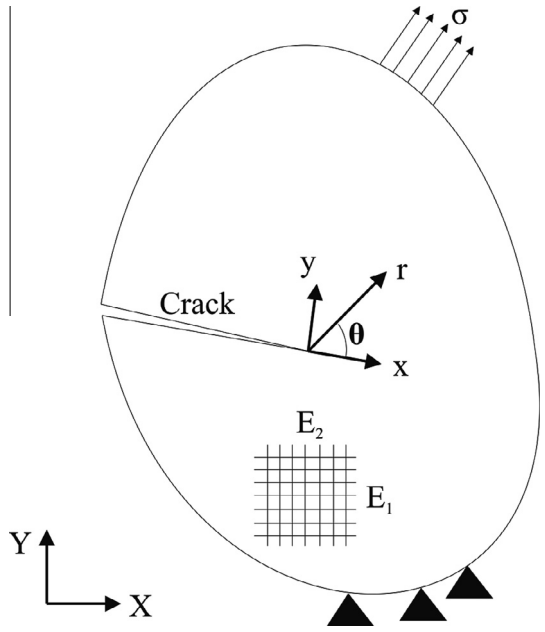

Fig. 2. A cracked orthotropic medium.

where m is the number of tip enrichment functions and nt is the number of nodes enriched by the crack tip functions, while $\mathbf{b}_i^j, b_{\alpha i}^j$ and $b_{\beta i}^j$ are additional degrees of freedom, presented as

$$\mathbf{t} = \{b_i^u, b_i^v, b_i^w, b_{\alpha i}, b_{\beta i}\}^T \tag{12}$$

In Eq. (11), F, G and R are the in-plane, out of plane and rotational tip enrichment functions, respectively [32]. Isotropic and orthotropic in-plane tip enrichment functions are considered for isotropic and composite problems, respectively.

According to [28], the following in-plane orthotropic tip enrichment functions are considered

$$F(r,\theta) = \left\{ \begin{array}{l} \sqrt{r}\cos\left(\frac{\theta_1}{2}\right)\sqrt{g_1(\theta)}, \sqrt{r}\cos\left(\frac{\theta_2}{2}\right)\sqrt{g_2(\theta)}, \\ \sqrt{r}\sin\left(\frac{\theta_1}{2}\right)\sqrt{g_1(\theta)}, \sqrt{r}\sin\left(\frac{\theta_2}{2}\right)\sqrt{g_2(\theta)} \end{array} \right\} \tag{13}$$

$$g_j(\theta) = \left(\left(\cos(\theta) + \gamma_j \sin(\theta)\right)^2 + \left(\beta_j \sin(\theta)\right)^2 \right)^{1/2}, \quad j = 1,2 \tag{14}$$

$$\theta_k(\theta) = \arctan\left(\frac{\beta_k sin(\theta)}{\cos(\theta) + \gamma_k sin(\theta)}\right), \quad k = 1,2 \tag{15}$$

where γ_j and β_j are obtained from the roots of the following characteristic equation [44]

$$p_{11}^{tip}\mu^4 - 2p_{16}^{tip}\mu^3 + \left(2p_{12}^{tip} + p_{66}^{tip}\right)\mu^2 - 2p_{26}^{tip}\mu + p_{22}^{tip} = 0 \tag{16}$$

$$\begin{array}{l} \mu_1 = \gamma_1 + i\beta_1 \\ \mu_2 = \gamma_2 + i\beta_2 \end{array} \tag{17}$$

and p_{ij} are the components of the compliance tensor $\mathbf{p}$ which is computed from the tensor of material properties $\mathbf{C}$,

$$\mathbf{C} = \begin{bmatrix} C_{11} & C_{12} & C_{13} & 0 & 0 & 0 \\ C_{21} & C_{22} & C_{23} & 0 & 0 & 0 \\ C_{31} & C_{32} & C_{33} & 0 & 0 & 0 \\ 0 & 0 & 0 & C_{44} & 0 & 0 \\ 0 & 0 & 0 & 0 & C_{55} & 0 \\ 0 & 0 & 0 & 0 & 0 & C_{66} \end{bmatrix} \tag{18}$$

$$\mathbf{p} = \mathbf{C}^{-1} \tag{19}$$

In the case of isotropic problems, the classical in-plane isotropic tip enrichment functions are employed [42]

$$F(r,\theta) = \left\{ \sqrt{r}\sin\left(\frac{\theta}{2}\right), \sqrt{r}\cos\left(\frac{\theta}{2}\right), \sqrt{r}\sin\left(\frac{\theta}{2}\right)\sin(\theta), \sqrt{r}\cos\left(\frac{\theta}{2}\right)\sin(\theta) \right\} \tag{20}$$

Out of plane and rotational enrichment functions are [32]

$$G(r,\theta) = \left\{ \sqrt{r}\sin\left(\frac{\theta}{2}\right), r^{3/2}\sin\left(\frac{\theta}{2}\right), r^{3/2}\cos\left(\frac{\theta}{2}\right), r^{3/2}\sin\left(\frac{3\theta}{2}\right), r^{3/2}\cos\left(\frac{3\theta}{2}\right) \right\} \tag{21}$$

$$R(r,\theta) = \left\{ \sqrt{r}\sin\left(\frac{\theta}{2}\right), \sqrt{r}\cos\left(\frac{\theta}{2}\right), \sqrt{r}\sin\left(\frac{\theta}{2}\right)\sin(\theta), \sqrt{r\cos\left(\frac{\theta}{2}\right)\sin(\theta)} \right\} \tag{22}$$

According to [32], without the loss of accuracy, the out plane enrichment functions can be further simplified to

$$G(r,\theta) = \left\{ \sqrt{r}\sin\left(\frac{\theta}{2}\right) \right\} \tag{23}$$

The total potential energy Π is used to derive the final form of the governing equation,

$$\Pi = \frac{1}{2}\int_v \boldsymbol{\varepsilon}_L^T \mathbf{C}\boldsymbol{\varepsilon}_L dV + \int_v \boldsymbol{\varepsilon}_{NL}^T \boldsymbol{\sigma}_0 dV \tag{24}$$

where $\mathbf{C}$ is the tensor of material properties, $\boldsymbol{\varepsilon}_L$ and $\boldsymbol{\varepsilon}_{NL}$ are the linear and nonlinear parts of Green–Lagrange strain,

$$\boldsymbol{\varepsilon} = \boldsymbol{\varepsilon}_L + \boldsymbol{\varepsilon}_{NL} = \left\{ \varepsilon_x, \varepsilon_y, \varepsilon_z, \gamma_{xy}, \gamma_{xz}, \gamma_{yz} \right\}^T \tag{25}$$

$$\boldsymbol{\varepsilon}_L = \frac{1}{2}\left(\frac{\partial \underset{\sim}{\mathbf{u}}_i}{\partial x_j} + \frac{\partial \underset{\sim}{\mathbf{u}}_j}{\partial x_i} \right) \tag{26}$$

$$\boldsymbol{\varepsilon}_{NL} = \frac{1}{2}\frac{\partial \underset{\sim}{\mathbf{u}}_k}{\partial x_i}\frac{\partial \underset{\sim}{\mathbf{u}}_k}{\partial x_j}, \quad i,j,k = 1,2,3 \tag{27}$$

where the indices 1, 2 and 3 are related to x, y and z directions, respectively. $\boldsymbol{\sigma}_0$ is the stress state computed from the linear static analysis,

$$\boldsymbol{\sigma}_0 = \{\sigma_{x0}, \sigma_{y0}, \sigma_{z0}, \tau_{xy0}, \tau_{yz0}, \tau_{xz0}\}^T \tag{28}$$

$\boldsymbol{\sigma}_0$ is then used to evaluate the geometric stiffness matrix, associated with the second part of Π.

Satisfying the principle of minimum potential energy requires the variation of Π to vanish ($\delta\Pi = 0$). After some manipulation, the stability equation is obtained as

$$(\mathbf{K} + \lambda \mathbf{K}_G)\{\mathbf{D}\} = \mathbf{0} \tag{29}$$

Eq. (29) is an eigenvalue equation, where λ represents the eigenvalue and $\mathbf{D}$ is the corresponding eigenvector; the buckling mode shapes,

$$\mathbf{D} = \left\{ \underset{\sim}{\mathbf{d}} \quad \mathbf{h} \quad \mathbf{t}_1 \quad \mathbf{t}_2 \quad \mathbf{t}_3 \quad \mathbf{t}_4 \right\}^T$$

The smallest value of λ determines the critical buckling stress. $\mathbf{K}$ and $\mathbf{K}_G$ are the standard and geometric stiffness matrices, respectively,

$$\mathbf{K}_{ij}^{rs} = \int_v (\mathbf{B}_i^r)^T \mathbf{C}\mathbf{B}_j^s dV \tag{30}$$

$$\mathbf{K}_{G\ ij}^{rs} = \int_v (\mathbf{B}_{G\ i}^r)^T \mathbf{S}_0 (\mathbf{B}_{G\ j}^s) dV \quad (r,s = \mathbf{d}, \mathbf{h}, \mathbf{t}) \tag{31}$$

and $\mathbf{S}_0$ is the matrix of stress components of $\boldsymbol{\sigma}_0$, computed from the static analysis

$$\mathbf{S}_0 = \begin{bmatrix} \bar{\mathbf{S}}_0 & \mathbf{0} & \mathbf{0} \\ \mathbf{0} & \bar{\mathbf{S}}_0 & \mathbf{0} \\ \mathbf{0} & \mathbf{0} & \bar{\mathbf{S}}_0 \end{bmatrix} \tag{32}$$

$$\bar{\mathbf{S}}_0 = \begin{bmatrix} \sigma_{x0} & \tau_{xy0} & \tau_{xz0} \\ \tau_{xy0} & \sigma_{y0} & \tau_{yz0} \\ \tau_{xz0} & \tau_{yz0} & \sigma_{z0} \end{bmatrix} \tag{33}$$

$\mathbf{B}^d$ can be obtained from [45]

$$\mathbf{B}_i^{\mathbf{d}} = \begin{bmatrix} \frac{\partial N_i}{\partial x} & 0 & 0 & \frac{\partial}{\partial x}\left(-\frac{\zeta t}{2} e_{x1} N_i\right) & \frac{\partial}{\partial x}\left(\frac{\zeta t}{2} e_{y1} N_i\right) \\ 0 & \frac{\partial N_i}{\partial y} & 0 & \frac{\partial}{\partial y}\left(-\frac{\zeta t}{2} e_{x2} N_i\right) & \frac{\partial}{\partial y}\left(\frac{\zeta t}{2} e_{y2} N_i\right) \\ 0 & 0 & \frac{\partial N_i}{\partial z} & \frac{\partial}{\partial z}\left(-\frac{\zeta t}{2} e_{x3} N_i\right) & \frac{\partial}{\partial z}\left(\frac{\zeta t}{2} e_{y3} N_i\right) \\ \frac{\partial N_i}{\partial y} & \frac{\partial N_i}{\partial x} & 0 & \frac{\partial}{\partial y}\left(-\frac{\zeta t}{2} e_{x1} N_i\right) + \frac{\partial}{\partial x}\left(-\frac{\zeta t}{2} e_{x2} N_i\right) & \frac{\partial}{\partial y}\left(\frac{\zeta t}{2} e_{y1} N_i\right) + \frac{\partial}{\partial x}\left(\frac{\zeta t}{2} e_{y2} N_i\right) \\ 0 & \frac{\partial N_i}{\partial z} & \frac{\partial N_i}{\partial y} & \frac{\partial}{\partial z}\left(-\frac{\zeta t}{2} e_{x2} N_i\right) + \frac{\partial}{\partial y}\left(-\frac{\zeta t}{2} e_{x3} N_i\right) & \frac{\partial}{\partial z}\left(\frac{\zeta t}{2} e_{y2} N_i\right) + \frac{\partial}{\partial y}\left(\frac{\zeta t}{2} e_{y3} N_i\right) \\ \frac{\partial N_i}{\partial z} & 0 & \frac{\partial N_i}{\partial x} & \frac{\partial}{\partial z}\left(-\frac{\zeta t}{2} e_{x1} N_i\right) + \frac{\partial}{\partial x}\left(-\frac{\zeta t}{2} e_{x3} N_i\right) & \frac{\partial}{\partial z}\left(\frac{\zeta t}{2} e_{y1} N_i\right) + \frac{\partial}{\partial x}\left(\frac{\zeta t}{2} e_{y3} N_i\right) \end{bmatrix} \tag{34}$$

To obtain the components of $\mathbf{B}_i^{\mathbf{h}}$, N_i should be replaced with $N_i(H(\mathbf{x}) - H(\mathbf{x}_i))$ in Eq. (34).

$\mathbf{B}^t$ is composed of four components,

$$\mathbf{B}_i^{\mathbf{t}} = \begin{bmatrix} \mathbf{B}_i^{\mathbf{t}1} & \mathbf{B}_i^{\mathbf{t}2} & \mathbf{B}_i^{\mathbf{t}3} & \mathbf{B}_i^{\mathbf{t}4} \end{bmatrix} \tag{35}$$

and each component $\mathbf{B}_i^{\mathbf{t}j}$, which is related to one of the specific tip enrichment functions, is computed as

$$\mathbf{B}_i^{\mathbf{t}} = \begin{bmatrix} \frac{\partial \phi}{\partial x} & 0 & 0 & \frac{\partial}{\partial x}\left(-\frac{\zeta t}{2} e_{x1} \varphi\right) & \frac{\partial}{\partial x}\left(\frac{\zeta t}{2} e_{y1} \varphi\right) \\ 0 & \frac{\partial \phi}{\partial y} & 0 & \frac{\partial}{\partial y}\left(-\frac{\zeta t}{2} e_{x2} \varphi\right) & \frac{\partial}{\partial y}\left(\frac{\zeta t}{2} e_{y2} \varphi\right) \\ 0 & 0 & \frac{\partial \kappa}{\partial z} & \frac{\partial}{\partial z}\left(-\frac{\zeta t}{2} e_{x3} \varphi\right) & \frac{\partial}{\partial z}\left(\frac{\zeta t}{2} e_{y3} \varphi\right) \\ \frac{\partial \phi}{\partial y} & \frac{\partial \phi}{\partial x} & 0 & \frac{\partial}{\partial y}\left(-\frac{\zeta t}{2} e_{x1} \varphi\right) + \frac{\partial}{\partial x}\left(-\frac{\zeta t}{2} e_{x2} \varphi\right) & \frac{\partial}{\partial y}\left(\frac{\zeta t}{2} e_{y1} \varphi\right) + \frac{\partial}{\partial x}\left(\frac{\zeta t}{2} e_{y2} \varphi\right) \\ 0 & \frac{\partial \phi}{\partial z} & \frac{\partial \kappa}{\partial y} & \frac{\partial}{\partial z}\left(-\frac{\zeta t}{2} e_{x2} \varphi\right) + \frac{\partial}{\partial y}\left(-\frac{\zeta t}{2} e_{x3} \varphi\right) & \frac{\partial}{\partial z}\left(\frac{\zeta t}{2} e_{y2} \varphi\right) + \frac{\partial}{\partial y}\left(\frac{\zeta t}{2} e_{y3} \varphi\right) \\ \frac{\partial \phi}{\partial z} & 0 & \frac{\partial \kappa}{\partial x} & \frac{\partial}{\partial z}\left(-\frac{\zeta t}{2} e_{x1} \varphi\right) + \frac{\partial}{\partial x}\left(-\frac{\zeta t}{2} e_{x3} \varphi\right) & \frac{\partial}{\partial z}\left(\frac{\zeta t}{2} e_{y1} \varphi\right) + \frac{\partial}{\partial x}\left(\frac{\zeta t}{2} e_{y3} \varphi\right) \end{bmatrix} \tag{36}$$

where ϕ, φ and κ are

$$\phi = N_i(F_j(\mathbf{x}) - F_j(\mathbf{x}_i)) \tag{37}$$

$$\varphi = N_i(R_j(\mathbf{x}) - R_j(\mathbf{x}_i)) \tag{38}$$

$$\kappa = N_i(G_j(\mathbf{x}) - G_j(\mathbf{x}_i)) \tag{39}$$

The geometric matrix $\mathbf{B}_{Gi}^{\mathbf{d}}$ can be written as [45],

$$\mathbf{B}_{Gi}^{\mathbf{d}} = \begin{bmatrix} \frac{\partial N_i}{\partial x} & 0 & 0 & \frac{\partial}{\partial x}\left(-\frac{\zeta t}{2} e_{x1} N_i\right) & \frac{\partial}{\partial x}\left(\frac{\zeta t}{2} e_{y1} N_i\right) \\ \frac{\partial N_i}{\partial y} & 0 & 0 & \frac{\partial}{\partial y}\left(-\frac{\zeta t}{2} e_{x1} N_i\right) & \frac{\partial}{\partial y}\left(\frac{\zeta t}{2} e_{y1} N_i\right) \\ \frac{\partial N_i}{\partial z} & 0 & 0 & \frac{\partial}{\partial z}\left(-\frac{\zeta t}{2} e_{x1} N_i\right) & \frac{\partial}{\partial z}\left(\frac{\zeta t}{2} e_{y1} N_i\right) \\ 0 & \frac{\partial N_i}{\partial x} & 0 & \frac{\partial}{\partial x}\left(-\frac{\zeta t}{2} e_{x2} N_i\right) & \frac{\partial}{\partial x}\left(\frac{\zeta t}{2} e_{y2} N_i\right) \\ 0 & \frac{\partial N_i}{\partial y} & 0 & \frac{\partial}{\partial y}\left(-\frac{\zeta t}{2} e_{x2} N_i\right) & \frac{\partial}{\partial y}\left(\frac{\zeta t}{2} e_{y2} N_i\right) \\ 0 & \frac{\partial N_i}{\partial z} & 0 & \frac{\partial}{\partial z}\left(-\frac{\zeta t}{2} e_{x2} N_i\right) & \frac{\partial}{\partial z}\left(\frac{\zeta t}{2} e_{y2} N_i\right) \\ 0 & 0 & \frac{\partial N_i}{\partial x} & \frac{\partial}{\partial x}\left(-\frac{\zeta t}{2} e_{x3} N_i\right) & \frac{\partial}{\partial x}\left(\frac{\zeta t}{2} e_{y3} N_i\right) \\ 0 & 0 & \frac{\partial N_i}{\partial y} & \frac{\partial}{\partial y}\left(-\frac{\zeta t}{2} e_{x3} N_i\right) & \frac{\partial}{\partial y}\left(\frac{\zeta t}{2} e_{y3} N_i\right) \\ 0 & 0 & \frac{\partial N_i}{\partial z} & \frac{\partial}{\partial z}\left(-\frac{\zeta t}{2} e_{x3} N_i\right) & \frac{\partial}{\partial z}\left(\frac{\zeta t}{2} e_{y3} N_i\right) \end{bmatrix} \tag{40}$$

$\mathbf{B}_{Gi}^{\mathbf{h}}$ is determined by replacing N_i with $N_i(H(\mathbf{x}) - H(\mathbf{x}_i))$ in Eq. (40), and $\mathbf{B}_{Gi}^{\mathbf{t}}$ is obtained as

$$\mathbf{B}_{Gi}^{\mathbf{t}} = \begin{bmatrix} \frac{\partial \phi}{\partial x} & 0 & 0 & \frac{\partial}{\partial x}\left(-\frac{\zeta t}{2} e_{x1} \varphi\right) & \frac{\partial}{\partial x}\left(\frac{\zeta t}{2} e_{y1} \varphi\right) \\ \frac{\partial \phi}{\partial y} & 0 & 0 & \frac{\partial}{\partial y}\left(-\frac{\zeta t}{2} e_{x1} \varphi\right) & \frac{\partial}{\partial y}\left(\frac{\zeta t}{2} e_{y1} \varphi\right) \\ \frac{\partial \phi}{\partial z} & 0 & 0 & \frac{\partial}{\partial z}\left(-\frac{\zeta t}{2} e_{x1} \varphi\right) & \frac{\partial}{\partial z}\left(\frac{\zeta t}{2} e_{y1} \varphi\right) \\ 0 & \frac{\partial \phi}{\partial x} & 0 & \frac{\partial}{\partial x}\left(-\frac{\zeta t}{2} e_{x2} \varphi\right) & \frac{\partial}{\partial x}\left(\frac{\zeta t}{2} e_{y2} \varphi\right) \\ 0 & \frac{\partial \phi}{\partial y} & 0 & \frac{\partial}{\partial y}\left(-\frac{\zeta t}{2} e_{x2} \varphi\right) & \frac{\partial}{\partial y}\left(\frac{\zeta t}{2} e_{y2} \varphi\right) \\ 0 & \frac{\partial \phi}{\partial z} & 0 & \frac{\partial}{\partial z}\left(-\frac{\zeta t}{2} e_{x2} \varphi\right) & \frac{\partial}{\partial z}\left(\frac{\zeta t}{2} e_{y2} \varphi\right) \\ 0 & 0 & \frac{\partial \kappa}{\partial x} & \frac{\partial}{\partial x}\left(-\frac{\zeta t}{2} e_{x3} \varphi\right) & \frac{\partial}{\partial x}\left(\frac{\zeta t}{2} e_{y3} \varphi\right) \\ 0 & 0 & \frac{\partial \kappa}{\partial y} & \frac{\partial}{\partial y}\left(-\frac{\zeta t}{2} e_{x3} \varphi\right) & \frac{\partial}{\partial y}\left(\frac{\zeta t}{2} e_{y3} \varphi\right) \\ 0 & 0 & \frac{\partial \kappa}{\partial z} & \frac{\partial}{\partial z}\left(-\frac{\zeta t}{2} e_{x3} \varphi\right) & \frac{\partial}{\partial z}\left(\frac{\zeta t}{2} e_{y3} \varphi\right) \end{bmatrix} \tag{41}$$

Evaluation of standard and geometric stiffness matrices, $\mathbf{K}$ and $\mathbf{K}_G$, requires accurate integration of Eqs. (30) and (31). Among several methods for numerical evaluation of these integrals [16,46–50], the sub-triangulation technique along with the Gauss quadrature rule is adopted in this study [43]. For elements enriched with the Heaviside function, 7 Gauss points are used in each triangle. In the tip elements, due to the presence of stress singularity in the vicinity of crack tip, 13 Gauss points are employed per triangle. For other elements, an ordinary 2×2 Gaussian quadrature rule is considered. The two different type of tip and split elements and their corresponding enriched nodes are shown in Fig. 3.

3. Numerical examples

In this section, linear eigenvalue buckling analyses are performed for five different problems in two cases of isotropic and orthotropic uni-layer composite plates. The effects of different parameters such as the aspect ratio, boundary conditions, crack length, crack angle and orthotropic angle on the buckling load and mode shapes are investigated. The problems include a cracked rectangular plate under uniform compressive, tensile and shear loading conditions, circular cracked plate with two concentrated tensile point loads and a square plate with two parallel cracks under tensile loading. Due to the fact that there is no documented information on the buckling of cracked fiber composite plates, the method is first verified for the isotropic cases available in the literature and then comprehensively examined for orthotropic problems.

For discretizing the model, eight-noded degenerated shell elements are considered and the reduced integration technique is adopted to avoid potential shear locking. Two sets of in-plane tip enrichment functions, Eqs. (13) and (20), are used for the orthotropic and isotropic problems, respectively.

The adopted mechanical properties for all orthotropic composite problems considered in this study are presented in Table 1. In

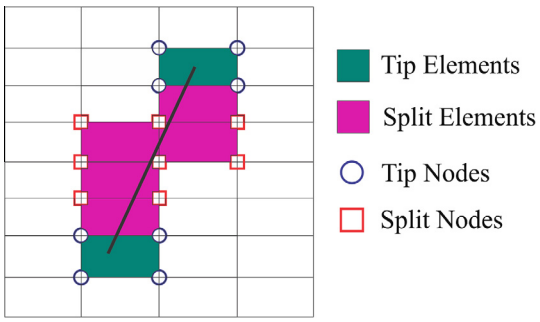

Fig. 3. Different element types and enriched nodes.

Table 1
Mechanical properties of composite material.

E_1(MPa)	E_2(MPa)	E_3(MPa)	G_{12}(MPa)	G_{13}(MPa)	G_{23}(MPa)	v_{12}	v_{13}	v_{23}
206842	20684.2	20684.2	6894.7	6894.7	4136.8	0.3	0.25	0.25

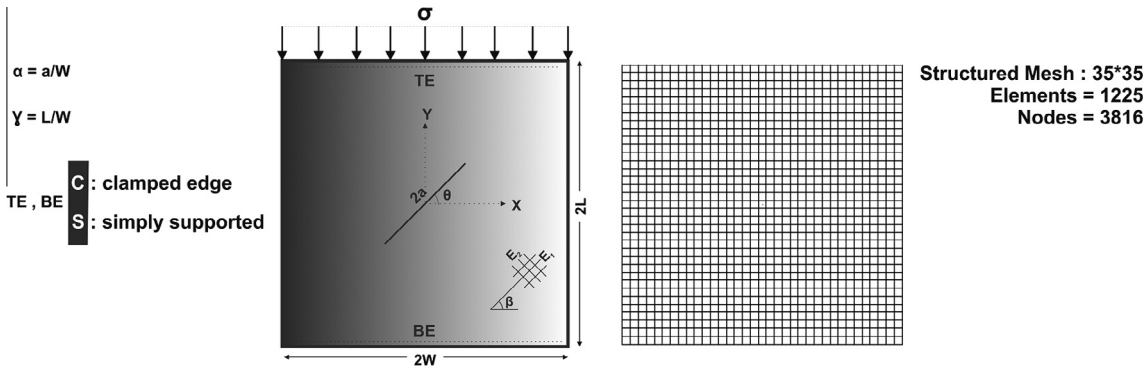

Fig. 4. Geometry and mesh of the plate.

Table 2
Critical buckling loads for the isotropic plate subjected to compressive loading.

γ	α	BC	θ°	Mode I buckling load (N)			Error %	
				EXP. [12]	FEM. [12]	XFEM	FEM	XFEM
1	0.1	CC	0	1627	1765.8	1682.3	8.5	3.4
1	0.3	CC	0	1531	1602.5	1560.8	4.7	2
1	0.3	CC	30	1551	1669.7	1630.1	7.7	5.1
1	0.5	CC	60	1636	1701.3	1694.9	4	3.6
1	0.5	CC	90	1665	1765.8	1738.3	6.1	4.4
1.33	0.3	CC	0	1158	1217.7	1191.6	5.2	2.9
2	0.5	CC	30	725	792.7	754	9.3	4
1	0.3	SC	0	815	835.7	833.8	2.5	2.3
1	0.3	SS	0	404	384.9	406.3	−4.7	0.6
1	0.5	SS	30	387	359.2	390.5	−7.2	0.9

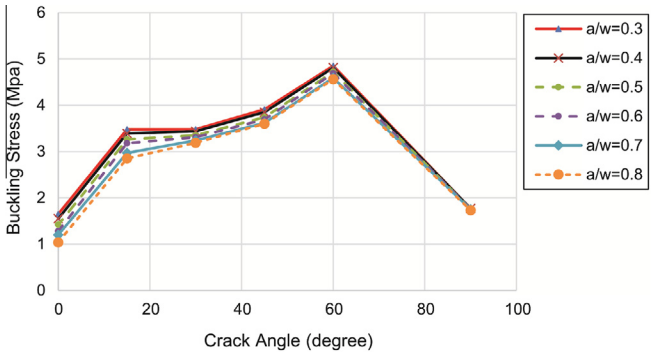

Fig. 5. Effect of the crack angle on the buckling stress.

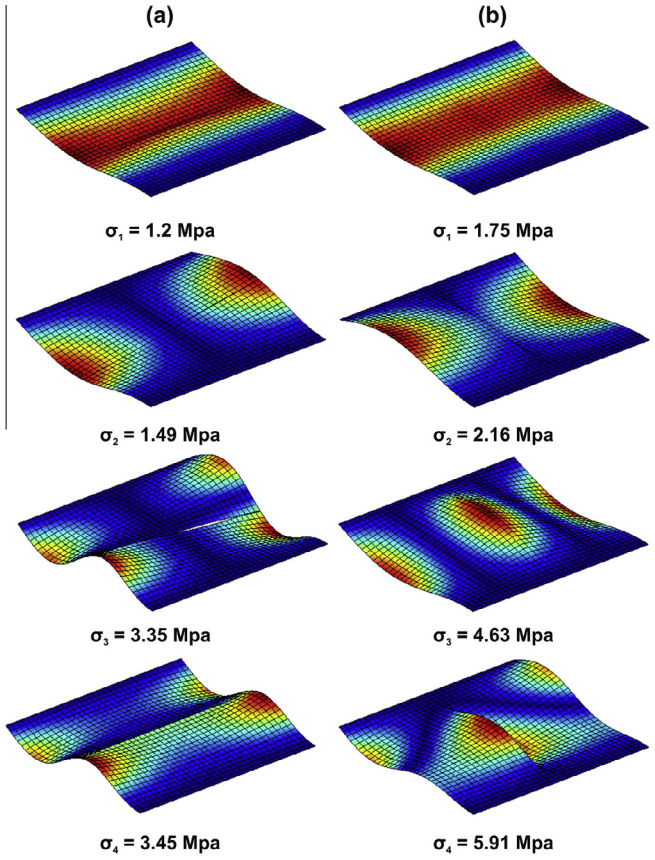

Fig. 6. The first four buckling mode shapes for the horizontally (a) and vertically (b) cracked composite plates.

the case of isotropic problems, the mechanical properties are defined separately for each problem.

3.1. Cracked rectangular plate under compression

3.1.1. Isotropic plate

A cracked rectangular plate subjected to a uniform in-plane compressive load was tested experimentally by Seifi and Khoda-yari [15] and then numerically simulated by the classical finite element method. The geometry of plate and loading condition as well as the typical structured finite element mesh (1225 elements) are shown in Fig. 4. Thickness of the plate is $t = 1.2$ mm, $E = 70$ GPa and $v = 0.3$. The extended finite element method with isotropic crack tip enrichment functions is adopted to perform the numerical simulations.

Four different boundary conditions are considered for plate edges. In all cases, the right and left edges of rectangular plates are free, whereas the other edges are either clamped (C) or simply supported (S), as depicted in Fig. 4.

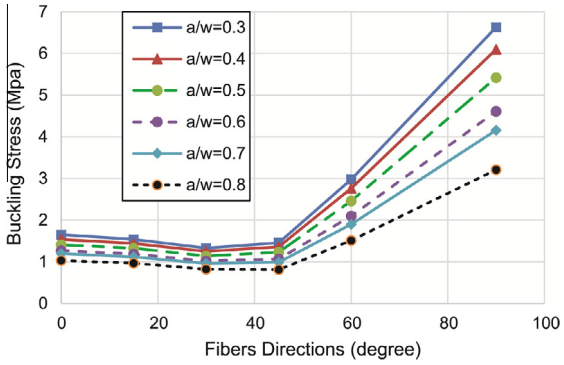

Fig. 7. Effect of orthotropic angle on the buckling stresses.

Table 2 compares the predicted critical stresses associated with the first mode of buckling for different cases of crack lengths and angles, aspect ratios and boundary conditions.

Clearly, the buckling loads predicted by XFEM are in better agreement with the experimental results. All simulations have been performed on a fixed mesh of 1225 elements and 3816 nodes, showing the efficiency of the present extended finite element modeling in comparison with the classical finite element method. It should be noted that Ref. [15] used 2157 elements and 6603 nodes to model the case of $\gamma = 1$, $\alpha = 0.3, \theta = 0^\circ$ and CC boundary conditions; almost two times the number of DOFs of present XFEM.

3.1.2. Orthotropic composite plate

In this section, buckling stresses for cracked orthotropic plates subjected to uniform compression are computed using a linear eigenvalue buckling analysis. Similarly, the effects of crack length and angle, direction of fibers and the aspect ratio of plate on the buckling stresses and mode shapes are studied and discussed in detail. It should be mentioned that the in-plane orthotropic enrichment functions are applied for modeling the stress singularity at the crack tip.

Effect of crack angle

First, the major orthotropic direction is assumed in the x direction and then the crack angle is changed. The plate dimensions are $W = L = 240$ mm, the thickness is $t = 1$ mm and the boundary condition is SC.

According to Fig. 5, increasing the crack length leads to reduction of buckling stress, e.g. the buckling stress for $a/W = 0.3$ is 1.58 times greater than the case of $a/W = 0.8$. In addition, increasing the angle of crack increases the buckling stress up to $\theta = 60^\circ$ and then decreases.

To investigate the effect of crack angle on the buckling mode shapes, the first four mode shapes corresponding to $\theta = 0^\circ$ and $\theta = 90^\circ$ cracks ($\alpha = 0.7$) and their associated buckling stresses are shown in Fig. 6. Clearly, the crack angle affects the buckling behavior of the plate so that in higher modes, the plate buckles in a dramatically different pattern.

Table 3
Critical buckling stresses for different crack lengths, aspect ratios and several fiber angles.

α	γ	β					
		0°	15°	30°	45°	60°	90°
		Mode I buckling stress (Mpa)					
0.3	1	1.65	1.54	1.33	1.46	2.98	6.63
0.3	1.33	1.63	1.51	1.26	1.34	2.82	6.39
0.3	2	1.61	1.49	1.17	1.19	2.7	6.34
0.8	1	1.03	0.97	0.82	0.81	1.51	3.21
0.8	1.33	1.12	1.05	0.88	0.89	1.67	3.22
0.8	2	1.22	1.13	0.91	0.92	1.91	4

Effect of orthotropic angle and the aspect ratio of plate

In this case, the crack angle is kept constant ($\theta = 0^\circ$), but the fibers orientation varies between $0^\circ \leqslant \beta \leqslant 90^\circ$. According to Fig. 7 the following conclusions can be made: for low fiber orientations, the buckling stresses are decreased with increasing the angle of fibers so that the most critical case is achieved at $\beta = 45^\circ$. Afterward, this attitude is reversed and with increasing the direction of fibers the buckling stresses are increased. Moreover, the buckling behavior is more sensitive to the orientation of the fibers after $\beta = 45^\circ$.

Table 3 compares the results of buckling stresses for two different horizontal crack lengths.

Expectedly, for small crack lengths ($\alpha = 0.3$), the buckling stress decreases when the aspect ratio is increased, whereas for long crack lengths ($\alpha = 0.8$) increasing the aspect ratio leads to the increase of the buckling stress.

In order to study the mesh sensitivity of results, several meshes with different number of elements are considered for the case of $\beta = 90^\circ, \theta = 0^\circ$ and $\alpha = 0.8$. The predicted buckling stresses, shown in Fig. 8, clearly indicate that by increasing the number of elements, a converged solution of 3.15 Mpa is obtained for the buckling stress.

3.2. Cracked rectangular plate under tension

A cracked rectangular plate subjected to tension can locally buckle around the crack faces due to existing local compressive stresses [12]. Seifi and Kabiri [14] evaluated the loads of isotropic plates experimentally and numerically by the classical finite element method. The geometry of the plate is shown in Fig. 4, and the analysis is performed for both isotropic and composite cases by a structured mesh of 1225 elements.

3.2.1. Isotropic plate

The mechanical material properties are similar to isotropic case of problem 3.1.1. The boundary conditions on the top and bottom edges are free and clamped (FC), respectively [14] and the thickness of the plate is $t = 1$ mm.

The critical buckling loads for different aspect ratios, crack lengths and angles are determined and presented in Table 4. Clearly, XFEM predicts more accurate results than the classical FEM. In addition, the present approach is more efficient because of using substantially less elements with a constant size of 6.8 mm, while, the reference was based on an extremely finer mesh with the maximum size of 3 mm and the minimum size of approximately 0.3 mm around the crack tip.

3.2.2. Orthotropic composite plate

Now, the same problem is solved for the orthotropic composite plate. The dimensions of the plate are $W = L = 240$ mm and

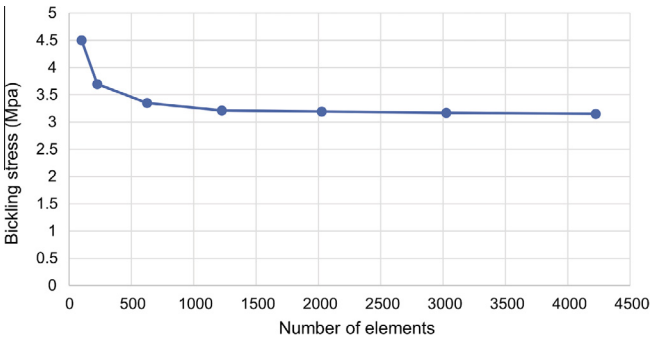

Fig. 8. Variation of the buckling stress for different mesh refinement.

Table 4
Critical buckling loads for the tensile isotropic plate for different values of aspect ratio, crack length and crack angle.

γ	α	θ	Buckling load (N)			Difference with EXP (%)	
			EXP. [11]	FEM. [11]	XFEM	FEM	XFEM
1	0.5	0	6361	6820.3	6694.6	6.7	2.1
1	0.6	15	4614.7	5204.6	4748.5	11.3	2.9
1	0.7	30	5592	5765.3	5697.2	3	1.9
1.3	0.5	0	8208.4	7998.7	8495.7	−2.6	3.5
1.3	0.6	15	6207.9	5897.3	6350.7	−5.3	2.3
1.3	0.7	30	5700.3	6220.8	5797.3	8.4	1.7

$t = 1$ mm. The mechanical properties are identical to Table 1. The effects of various parameters such as the crack length and angle, direction of fibers and different boundary conditions on the buckling stresses and mode shapes are investigated. Three types of boundary conditions are considered:

Type A: top and bottom edges are clamped, left and right edges are free.
Type B: top and bottom edges are clamped, left and right edges are restrained just for out of plane displacement and free for in-plane displacements.
Type C: similar to Type B except that the displacements in the x direction are restrained for the left and right edges.

Effect of crack length and orthotropic angle

Various crack lengths and orthotropic angles are considered in this section and their effects on the buckling stress are investigated, as shown in Fig. 9. Type A boundary condition is considered for the analyses.

It is observed that with increasing the crack length, the critical buckling stress is substantially decreased. Also, the buckling stress first varies in a decreasing trend up to $\beta = 45^\circ$ and then follows an increasing path with further increase of the angle of fibers.

The buckling mode shapes related to fiber orientations of $\beta = 0^\circ$ and $\beta = 30^\circ$ are presented in Fig. 10, which clearly shows that the angle of fibers can significantly change the buckling behavior of plate in different modes.

Effect of boundary condition and crack angle

Table 5 compares the buckling stresses for three different boundary conditions in terms of different crack angles. The results are obtained for $\alpha = 0.8, t = 1$ mm and $\beta = 0^\circ$. According to the results, no significance difference is observed between Type A and B because in these cases the local buckling of crack edges depends highly on the compressive in-plane stress distribution around the crack faces and the restraint condition of out of plane movements at edges of the plate does not largely affect the in-plane stress distribution under this loading condition. On the other hand, the effect of in-plane displacements at edges of the plate (Type C) can crucially affect the stress distribution around the crack faces and therefore, buckling stresses become totally different from the other types (Fig. 11).

In addition, the critical buckling stresses are dramatically increased by increasing the crack angle, as depicted in Fig. 11. Finally, it is noted that at $\theta = 90^\circ$ no compressive stress is generated in the present tensile configuration and the plate does not buckle, globally or locally.

From the presented results, it can be inferred that cracked composite plates are highly susceptible to buckling. Among the studied problems, the most vulnerable case is associated with the 45° inclined fibers. Therefore, necessary measures need to be considered for practical engineering designs. On the other hand, presence of appropriate supports at plate edges can significantly improve its buckling behavior.

3.3. Edge cracked shear panel

The buckling analysis of a cracked shear panel, previously studied by Alinia et al. [16], is considered, as shown in Fig. 12. They used denser adaptive mesh around the crack tip with the minimum size of approximately 0.5 mm and the maximum size of 25 mm for other regions, whereas here a uniform extended finite element mesh with the size of 28.6 mm is used for modeling the edge cracked shear panel. First, the isotropic case is studied and the linear eigenvalue buckling analysis is performed and the obtained results are compared with the reference results. Then, the orthotropic composite case is considered and the effects of different orthotropic angles and crack lengths on the buckling behavior of the plate are examined.

3.3.1. Isotropic plate

Similar to previous problems, a structured mesh with 1225 elements and 3816 nodes is adopted to discretize the model and to compute the buckling shear stress. Material properties, boundary

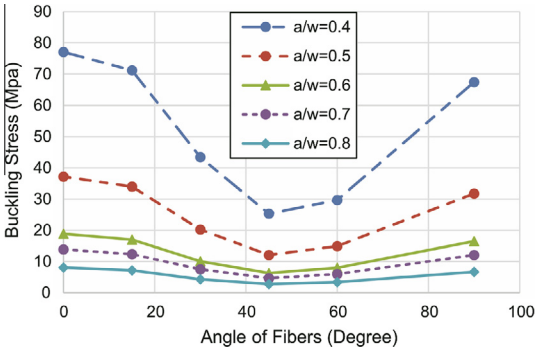

Fig. 9. Effect of fiber directions on the buckling stresses.

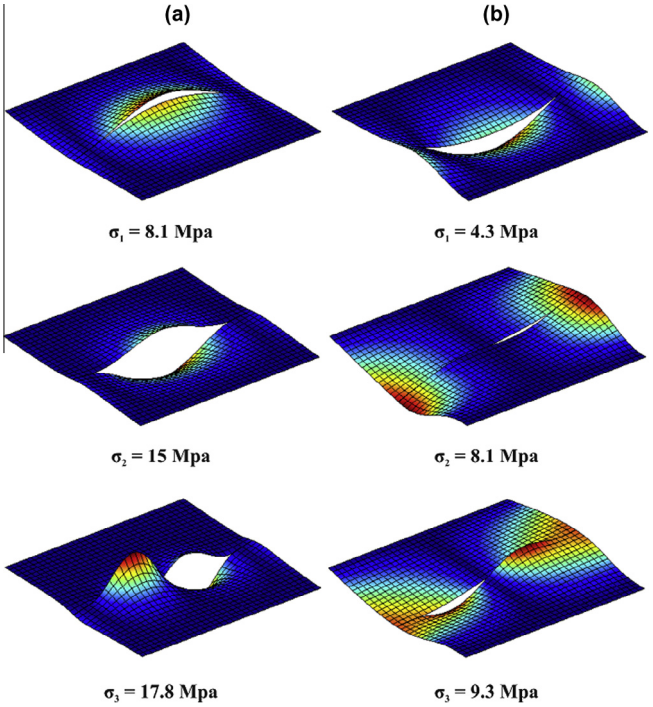

Fig. 10. The first three buckling mode shapes for (a)$\beta = 0^\circ$ and (b)$\beta = 30^\circ$.

Table 5
Buckling stresses for various crack angles and boundary conditions.

θ°	Buckling stress (Mpa)		
	Type A	Type B	Type C
0	8.3	10.0	61.2
15	8.5	9.1	96.2
30	14.0	14.3	130.4
45	20.6	21.3	159.6

condition and the dimensions of the plate are identical with [16], $W = L = 1000$ mm, $t = 3$ mm, $E = 210$ GPa and $\upsilon = 0.3$.

Comparison of the predicted results with the reference data, as illustrated in Fig. 13, shows a very good agreement. The reference results [16] used substantially more elements than the present method, showing the efficiency of the present XFEM.

3.3.2. Orthotropic plate

The same plate of Fig. 12 with dimensions of $L = W = 1000$ mm and $t = 3$ mm is considered. The material properties are according to Table 1. Linear eigenvalue buckling analysis is performed for the edge cracked panel and the effects of fiber orientation and crack length on the buckling shear stresses and mode shapes are investigated.

Variations of the buckling shear stress with respect to fiber directions are shown in Fig. 14, which shows a decreasing trend with the increasing angle up to $\beta = 45^\circ$. As a result, the buckling shear stress for the case of $a/W = 0.4$ and $\beta = 0^\circ$ is about 3 times greater than the case of $a/W = 0.7$. Moreover, the most critical fiber direction is related to $\beta = 45^\circ$, and when the fibers are parallel to the crack ($\beta = 90^\circ$), the buckling behavior is improved and the biggest buckling stress is achieved.

In order to show the effect of fiber directions on the buckling mode shapes, the first three buckling mode shapes for the case of $a/W = 0.7$ and angles of fibers $\beta = 0^\circ$ and $\beta = 90^\circ$ are presented in Fig. 15.

3.4. Buckling analysis of cracked composite circular plate

The other example is dedicated to a simply supported cracked composite circular plate subjected to two concentrated point loads. Earlier, this problem was considered by Asadpoure and Mohammadi [28] to calculate the static stress intensity factors for different crack orientations. Now, the buckling analysis of this problem is performed in the framework of extended finite element method. The material properties are similar to Table 1 and the ratio of the radius to the plate thickness is $R/t = 500$. The geometry and boundary conditions of the plate are shown in Fig. 16. An unstructured mesh composed of 2232 elements is adopted, as depicted in Fig. 16(b). The local buckling in tensile loading may occur at crack faces due to the generated local compressive stresses in these regions. It is illustrated that fiber orientation can have a significant effect on the buckling loads and mode shapes. Also, different angles of crack are taken into account and the sensitivity of the results are studied.

Fig. 17 illustrates the importance of fibers direction on the buckling load. The crack is considered horizontal and the direction of fibers varies from horizontal to vertical. Clearly, the buckling loads are substantially sensitive to the orientation of the fibers; for instance for the case of $a/2R = 0.6$, the critical buckling load for $\beta = 0^\circ$ is 3.8 times greater than the buckling load for $\beta = 90^\circ$. The most vulnerable case occurs when the fibers are perpendicular to the crack path ($\beta = 90^\circ$).

Also, a comparison is made for different crack angles to investigate the effect of crack orientation on the buckling load. For this purpose, the crack length is assumed constant $a/2R = 0.7$. The predicted buckling loads are shown in Fig. 18, which shows that the crack angle can significantly change the buckling behavior. A decrease of 52 % occurs in the buckling load for the case of $\beta = 0^\circ$, as the crack angle is increased from $\theta = 30^\circ$ to $\theta = 45^\circ$.

Finally, the buckling mode shapes for the case of a horizontal crack with $a/2R = 0.7$ and $\beta = 30^\circ$ are depicted in Fig. 19. Accordingly, the plate buckles locally only around the crack faces where the compressive stresses are generated even in global concentrated tensile point loadings.

3.5. Composite square plate with two parallel cracks

Due to the fact that XFEM formulation can handle problems of multiple cracks, the last example is dedicated to buckling analysis of a composite square plate with two parallel cracks under tensile loading, as shown in Fig. 20. The effects of crack length, distance between two cracks and different isotropic and orthotropic tip enrichment functions on the critical buckling stress are investigated. The dimensions of the plate are $W = 240$ mm and $t = 1$ mm and a 35×35 structured mesh is considered. The boundary conditions of the plate is similar to Type-A in Section 3.2.2, direction of the fibers are assumed parallel to the cracks and the material properties are similar to other composite examples.

The critical buckling stresses for different crack lengths and distances between the cracks are presented in Table 6. It is observed that increasing the crack length substantially affects the buckling behavior of plate. For example, in all cases, the buckling stresses for $a/W = 0.8$ are approximately 6 times lower than the case of $a/W = 0.5$. Also, with increasing the distance of cracks, at first,

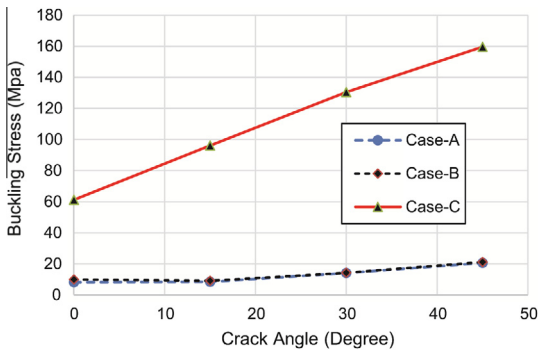

Fig. 11. Effect of crack angle and boundary conditions on the buckling stresses.

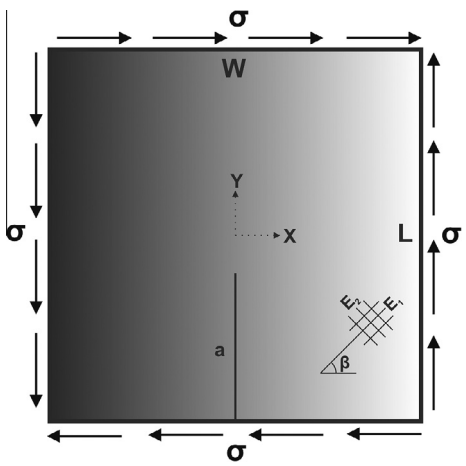

Fig. 12. Edge cracked plate subjected to shear loading.

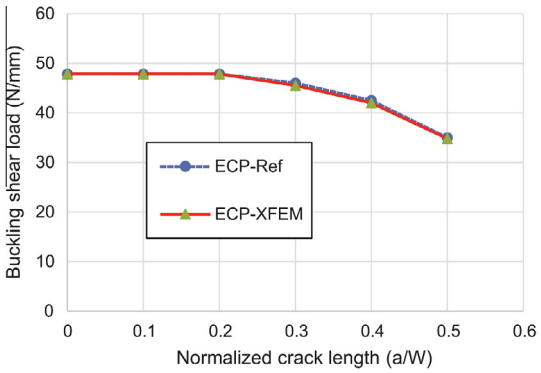

Fig. 13. Critical shear force with respect to the normalized crack length.

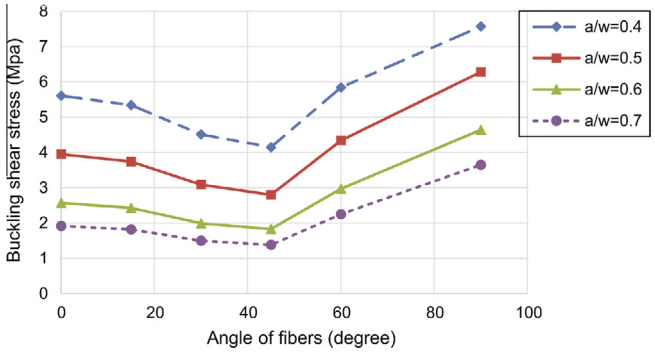

Fig. 14. Buckling shear stresses of the edge cracked panel for different crack lengths and fiber angles.

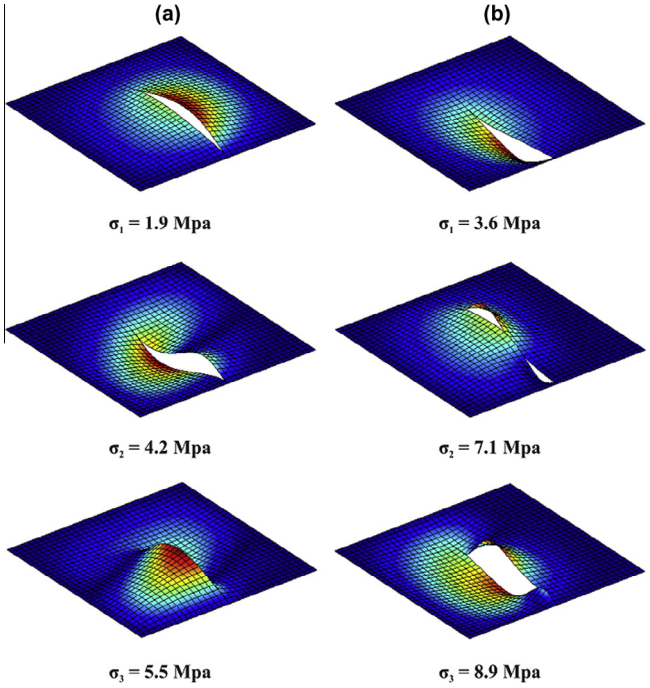

Fig. 15. The first three buckling mode shapes for the edge cracked plate subjected to shear loading for two different fiber orientations, (a) $\beta = 0^\circ$ and (b) $\beta = 90^\circ$.

the buckling stresses are increased up to $d/W = 0.1667$, and then decreased when the cracks approaching to the edges of the plate.

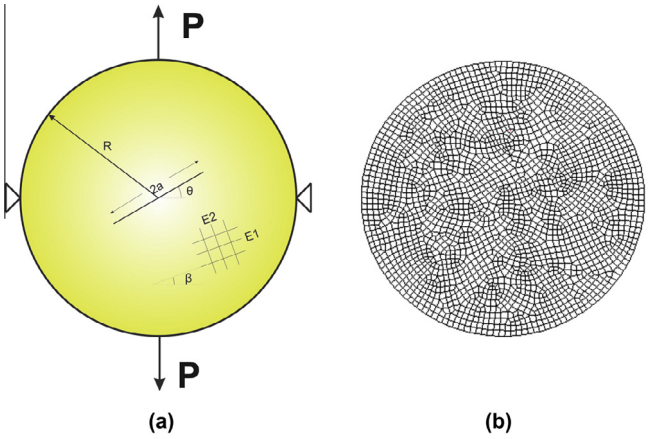

Fig. 16. Cracked composite circular plate (a) and the FE mesh (b).

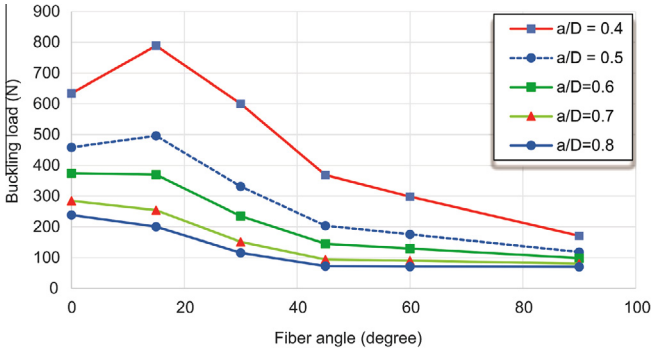

Fig. 17. Buckling loads versus fiber angles for different horizontal crack lengths.

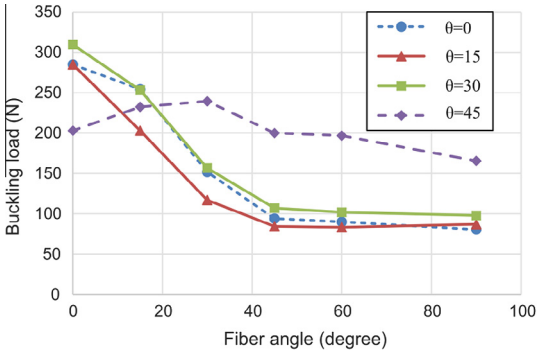

Fig. 18. Effect of crack angle and fiber direction on the buckling load.

In order to evaluate the effect of different crack tip enrichment functions on plate buckling response two sets of in-plane isotropic and orthotropic tip enrichment functions are considered and the results are presented in Table 7. It can be noted that with decreasing the distance of the cracks the difference between buckling stresses predicted by adopted isotropic and orthotropic tip enrichment functions are increased. The reason can be attributed to the fact that when two crack tips approach, they intensify the stress concentration in the neighborhood of the crack tips. Such a complex displacement field is better captured with the orthotropic tip enrichment functions, as their analytical bases are closer to the generated complex field.

The first four mode shapes of buckling for two different distances of cracks are depicted in Fig. 21. Clearly, it can be noted that

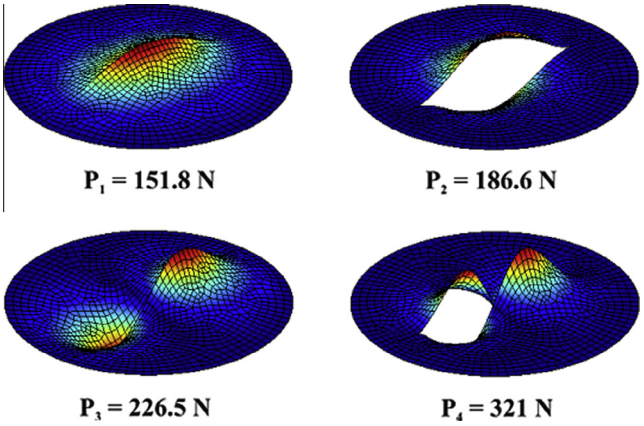

Fig. 19. Four buckling mode shapes of circular cracked composite plate.

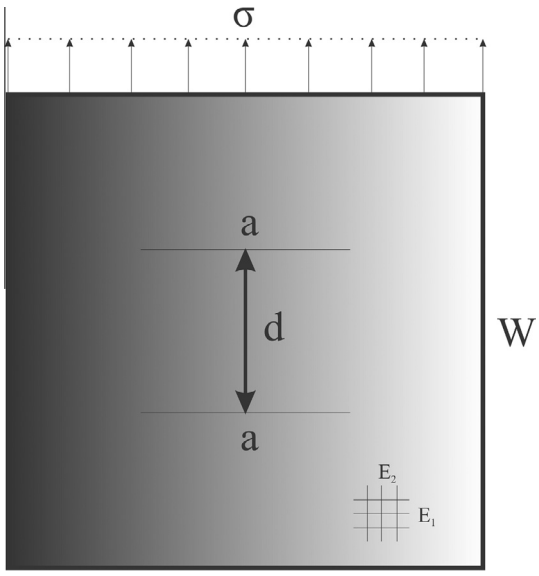

Fig. 20. Geometry of composite square plate with two parallel cracks.

Table 6
Tensile critical buckling stresses for various crack lengths and distance between two cracks.

d/W	a/W			
	0.5	0.6	0.7	0.8
	Mode I buckling stress (MPa)			
0.0417	47.03	21.40	10.87	7.20
0.0833	55.22	23.98	11.91	7.97
0.1667	62.48	27.50	13.65	9.26
0.3333	53.67	19.61	12.50	8.46

Table 7
Tensile buckling stresses for isotropic and orthotropic tip enrichments for various distance of cracks.

d/W	Mode I buckling stress (MPa)		
	Orthotropic enrichment	Isotropic enrichment	Difference (%)
0.0417	10.87	11.67	7.36
0.0833	11.91	12.67	6.38
0.1667	13.65	14.46	5.93
0.3333	12.5	13.09	4.72

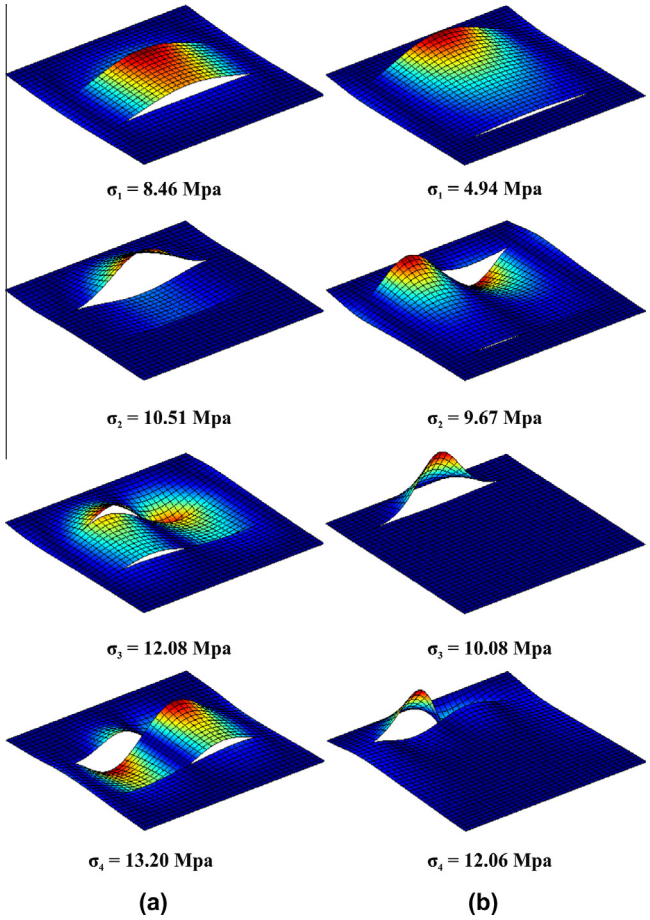

Fig. 21. The first four mode shapes of buckling composite plate with two parallel cracks for two different crack distances (a) d/W = 0.33 and (b) d/W = 0.66.

the distance of the cracks can significantly alter the modes of buckling, so that when two cracks getting closer, two sides of cracks buckle simultaneously, despite of the situation when the cracks are near the edges. Also, as mentioned before, when cracks approaching to the edges of the plate the buckling stresses decrease. Unfortunately, no reference solution is available for this complicated problem to be used for verification or comparison purposes.

4. Conclusion

Numerical buckling analysis has been performed in this study within the framework of the extended finite element method for various cracked composite plates. The effects of different parameters, such as crack length, crack angle and direction of the fiber on the buckling behavior of several cracked uni-layer composite plates have extensively been investigated. The following conclusions have been made:

- It is clearly demonstrated that the present method is more accurate and efficient than the classical finite element method. Even with substantially fewer elements, in some cases two times fewer, more accurate results are achieved.
- Generally, for all loading conditions, buckling stresses decrease with increasing the crack length. For example, when the plate is subjected to compressive loading, increasing the coefficient of crack length from $\gamma = 0.3$ to $\gamma = 0.8$ leads to 58 % reduction in the buckling stress. Also, the crack direction has a prominent

effect on the buckling behavior of the plate. For instance, in the tensile loading condition, when the crack is parallel to the direction of loading, the plate does not buckle.

- Fiber directions can significantly change the buckling behavior of the plate. For example, in the case of rectangular plate subjected to tensile loading, changing the fiber direction can alter the response from the local buckling mode around the crack faces to a global buckling mode. Also, according to the obtained results for the first three examples, it can be observed that the most vulnerable case occurs if the angle of fibers and crack path is $\beta = 45^{\circ}$.
- The present formulation can handle problems of multiple cracks without any additional difficulties.
- The effects of different isotropic and orthotropic tip enrichment functions on the buckling stresses have been studied. It is observed that when two crack tips approach, the difference between the critical buckling stresses increases. The reason can be attributed to the fact that when two crack tip approach, they intensify the stress concentration in the neighborhood of the crack tips. Such a complex displacement field is better captured with the orthotropic tip enrichment functions, as their analytical bases are chosen to the generated complex field.

Acknowledgments

The authors wish to gratefully acknowledge the technical support of the High Performance Computing Lab, School of Civil Engineering, University College of Engineering, University of Tehran. Furthermore, the financial support of Iran National Science Foundation (INSF) is gratefully acknowledged.

References

[1] Thai H-T, Kim S-E. Levy-type solution for buckling analysis of orthotropic plates based on two variable refined plate theory. Compos Struct 2011;93:1738–46.
[2] Lopatin A, Morozov E. Buckling of the SSFF rectangular orthotropic plate under in-plane pure bending. Compos Struct 2009;90:287–94.
[3] Bao G, Jiang W, Roberts J. Analytic and finite element solutions for bending and buckling of orthotropic rectangular plates. Int J Solids Struct 1997;34:1797–822.
[4] Lopatin A, Korbut Y. Buckling of clamped orthotropic plate in shear. Compos Struct 2006;76:94–8.
[5] Naderi A, Saidi A. An accurate approach for finding the critical buckling stress of thick orthotropic plates. Compos Struct 2013;96:411–8.
[6] Qiao P, Huo X. Explicit local buckling analysis of rotationally-restrained orthotropic plates under uniform shear. Compos Struct 2011;93:2785–94.
[7] Thai CH, Ferreira A, Bordas S, Rabczuk T, Nguyen-Xuan H. Isogeometric analysis of laminated composite and sandwich plates using a new inverse trigonometric shear deformation theory. Eur J Mech A/Solids 2014;43:89–108.
[8] Thai CH, Nguyen-Xuan H, Nguyen-Thanh N, Le TH, Nguyen-Thoi T, Rabczuk T. Static, free vibration, and buckling analysis of laminated composite Reissner–Mindlin plates using NURBS-based isogeometric approach. Int J Numer Methods Eng 2012;91:571–603.
[9] Valizadeh N, Natarajan S, Gonzalez-Estrada OA, Rabczuk T, Bui TQ, Bordas SP. NURBS-based finite element analysis of functionally graded plates: static bending, vibration, buckling and flutter. Compos Struct 2013;99:309–26.
[10] Markström K, StoÅkers B. Buckling of cracked members under tension. Int J Solids Struct 1980;16:217–29.
[11] Shaw D, Huang Y. Buckling behavior of a central cracked thin plate under tension. Eng Fract Mech 1990;35:1019–27.
[12] Riks E, Rankin C, Brogan F. The buckling behavior of a central crack in a plate under tension. Eng Fract Mech 1992;43:529–48.
[13] Vafai A, Javidruzi M, Estekanchi H. Parametric instability of edge cracked plates. Thin-walled Struct 2002;40:29–44.
[14] Seifi R, Kabiri AR. Lateral Load effects on buckling of cracked plates under tensile loading. Thin-walled Struct 2013;72:37–47.
[15] Seifi R, Khoda-yari N. Experimental and numerical studies on buckling of cracked thin-plates under full and partial compression edge loading. Thin-walled Struct 2011;49:1504–16.
[16] Alinia M, Hosseinzadeh S, Habashi H. Numerical modelling for buckling analysis of cracked shear panels. Thin-walled Struct 2007;45:1058–67.
[17] Guz A, Dyshel MS. Fracture and buckling of thin panels with edge crack in tension. Theor Appl Fract Mech 2001;36:57–60.
[18] Khedmati MR, Edalat P, Javidruzi M. Sensitivity analysis of the elastic buckling of cracked plate elements under axial compression. Thin-walled Struct 2009;47:522–36.
[19] Liu F-L. Differential quadrature element method for buckling analysis of rectangular Mindlin plates having discontinuities. Int J Solids Struct 2001;38:2305–21.
[20] Pan Z, Cheng Y, Liu J. A semi-analytical analysis of the elastic buckling of cracked thin plates under axial compression using actual non-uniform stress distribution. Thin-walled Struct 2013;73:229–41.
[21] Baiz P, Natarajan S, Bordas S, Kerfriden P, Rabczuk T. Linear buckling analysis of cracked plates by SFEM and XFEM. J Mech Mater Struct 2012;6:1213–38.
[22] Natarajan S, Baiz PM, Bordas S, Rabczuk T, Kerfriden P. Natural frequencies of cracked functionally graded material plates by the extended finite element method. Compos Struct 2011;93:3082–92.
[23] Nguyen-Thoi T, Rabczuk T, Lam-Phat T, Ho-Huu V, Phung-Van P. Free vibration analysis of cracked Mindlin plate using an extended cell-based smoothed discrete shear gap method (XCS-DSG3). Theor Appl Fract Mech 2014;72:150–63.
[24] Yu T, Bui TQ, Liu P, Hirose S. A stabilized discrete shear gap extended finite element for the analysis of cracked Reissner–Mindlin plate vibration problems involving distorted meshes. Int J Mech Mater Des 2014:1–23.
[25] Barut A, Madenci E, Britt V, Starnes Jr J. Buckling of a thin, tension-loaded, composite plate with an inclined crack. Eng Fract Mech 1997;58:233–48.
[26] Rad AA, Panahandeh-Shahraki D. Buckling of cracked functionally graded plates under tension. Thin-walled Struct 2014;84:26–33.
[27] Natarajan S, Chakraborty S, Ganapathi M, Subramanian M. A parametric study on the buckling of functionally graded material plates with internal discontinuities using the partition of unity method. Eur J Mech A/Solids 2014;44:136–47.
[28] Asadpoure A, Mohammadi S. Developing new enrichment functions for crack simulation in orthotropic media by the extended finite element method. Int J Numer Methods Eng 2007;69:2150–72.
[29] Asadpoure A, Mohammadi S, Vafai A. Crack analysis in orthotropic media using the extended finite element method. Thin-walled Struct 2006;44:1031–8.
[30] Asadpoure A, Mohammadi S, Vafai A. Modeling crack in orthotropic media using a coupled finite element and partition of unity methods. Finite Elem Anal Des 2006;42:1165–75.
[31] Ashari S, Mohammadi S. Delamination analysis of composites by new orthotropic bimaterial extended finite element method. Int J Nume Methods Eng 2011;86:1507–43.
[32] Bayesteh H, Mohammadi S. XFEM fracture analysis of shells: The effect of crack tip enrichments. Comput Mater Sci 2011;50:2793–813.
[33] Bayesteh H, Mohammadi S. XFEM fracture analysis of orthotropic functionally graded materials. Compos Part B: Eng 2013;44:8–25.
[34] Belytschko T, Moës N, Usui S, Parimi C. Arbitrary discontinuities in finite elements. Int J Numer Methods Eng 2001;50:993–1013.
[35] Dolbow J, Gosz M. On the computation of mixed-mode stress intensity factors in functionally graded materials. Int J Solids Struct 2002;39:2557–74.
[36] Motamedi D, Mohammadi S. Dynamic crack propagation analysis of orthotropic media by the extended finite element method. Int J Fract 2010;161:21–39.
[37] Motamedi D, Mohammadi S. Dynamic analysis of fixed cracks in composites by the extended finite element method. Eng Fract Mech 2010;77:3373–93.
[38] Motamedi D, Mohammadi S. Fracture analysis of composites by time independent moving-crack orthotropic XFEM. Int J Mech Sci 2012;54:20–37.
[39] Nguyen-Thanh N, Valizadeh N, Nguyen M, Nguyen-Xuan H, Zhuang X, Areias P, et al. An extended isogeometric thin shell analysis based on Kirchhoff–Love theory. Comput Methods Appl Mech Eng 2015;284:265–91.
[40] Rabczuk T, Areias P. A meshfree thin shell for arbitrary evolving cracks based on an extrinsic basis. 2006.
[41] Rabczuk T, Areias P, Belytschko T. A meshfree thin shell method for non-linear dynamic fracture. Int J Numer Methods Eng 2007;72:524–48.
[42] Mohammadi S. Extended finite element method: for fracture analysis of structures. John Wiley & Sons; 2008.
[43] Mohammadi S. XFEM fracture analysis of composites. John Wiley & Sons; 2012.
[44] Lekhnitskii S. Theory of elasticity of an anisotropic elastic body. San Francisco: Holden-Day; 1963.
[45] Cook RD. Concepts and applications of finite element analysis. John Wiley & Sons; 2007.
[46] Bordas S, Natarajan S, Kerfriden P, Augarde CE, Mahapatra DR, Rabczuk T, et al. On the performance of strain smoothing for quadratic and enriched finite element approximations (XFEM/GFEM/PUFEM). Int J Numer Methods Eng 2011;86:637–66.
[47] Mousavi S, Sukumar N. Numerical integration of polynomials and discontinuous functions on irregular convex polygons and polyhedrons. Comput Mech 2011;47:535–54.
[48] Natarajan S, Bordas S, Roy Mahapatra D. Numerical integration over arbitrary polygonal domains based on Schwarz–Christoffel conformal mapping. Int J Numer Methods Eng 2009;80:103–34.
[49] Natarajan S, Mahapatra DR, Bordas S. Integrating strong and weak discontinuities without integration subcells and example applications in an XFEM/GFEM framework. Int J Numer Methods Eng 2010;83:269–94.
[50] Ventura G, Gracie R, Belytschko T. Fast integration and weight function blending in the extended finite element method. Int J Numer Methods Eng 2009;77:1–29.